Energies **2015**, *8*, 6302-6327; doi:10.3390/en8076302

OPEN ACCESS

energies

ISSN 1996-1073

www.mdpi.com/journal/energies

Article

Power Management Optimization of an Experimental Fuel Cell/Battery/Supercapacitor Hybrid System

Farouk Odeim *, Jürgen Roes and Angelika Heinzel

Chair of Energy Technology, University of Duisburg-Essen, Lotharstr. 1, 47057 Duisburg, Germany; E-Mails: juergen.roes@uni-due.de (J.R.); angelika.heinzel@uni-due.de (A.H.)

* Author to whom correspondence should be addressed; E-Mail: farouk.odeim@stud.uni-due.de; Tel.: +49-203-379-1256; Fax: +49-203-379-2720.

Academic Editors: Joeri Van Mierlo and Omar Hegazy

Received: 13 March 2015 / Accepted: 15 June 2015 / Published: 25 June 2015

Abstract: In this paper, an experimental fuel cell/battery/supercapacitor hybrid system is investigated in terms of modeling and power management design and optimization. The power management strategy is designed based on the role that should be played by each component of the hybrid power source. The supercapacitor is responsible for the peak power demands. The battery assists the supercapacitor in fulfilling the transient power demand by controlling its state-of-energy, whereas the fuel cell system, with its slow dynamics, controls the state-of-charge of the battery. The parameters of the power management strategy are optimized by a genetic algorithm and Pareto front analysis in a framework of multi-objective optimization, taking into account the hydrogen consumption, the battery loading and the acceleration performance. The optimization results are validated on a test bench composed of a fuel cell system (1.2 kW, 26 V), lithium polymer battery (30 Ah, 37 V), and a supercapacitor (167 F, 48 V).

Keywords: fuel cell/battery/supercapacitor hybrid; power management; multi-objective optimization; durability; experimental validation

1. Introduction

The limited fossil fuel resources and the environmental concerns associated with burning those fossil fuels lie behind the increasing interest in hydrogen as a clean and sustainable alternative to fossil fuels,

and in fuel cells as a clean converter of hydrogen into electrical energy especially in the transportation sector. Even though fuel cell hybrid vehicles (FCHVs) have not yet entered the large scale commercialization phase, they have a great potential to be the final step in the transition of the transportation sector to the environmentally friendly vehicles [1].

FCHVs are characterized by the use of a fuel cell system (FCS) as the main power source and a supercapacitor, a battery or both as an energy storage system (ESS). In comparison to pure FCS powertrains, adding an ESS to form a hybrid powertrain is advantageous for the following main reasons: (1) FCSs exhibit slow dynamics and long start-up times; an ESS is needed to improve the responsiveness of the power source to abrupt load changes during acceleration; (2) in the hybrid system, the ESS helps meet the peak power demands, so that the FCS needs to be sized according to the cruising demand only, not to the peak demand as in pure FCS powertrains; (3) the ESS significantly improves the hydrogen economy by restricting the operation of the FCS to high-efficiency operating points and by adding the possibility of regenerative braking.

The durability is still the major challenge to fuel cell commercialization. For transportation applications, fuel cell systems are required to achieve a minimum lifetime of 5000 h to be comparable with the current automotive engines [2]. The load dynamics is considered as the main aging-accelerator [3]. Load changing leads to many degradation effects like flooding of the porous media of the electrodes, dehydration of the membrane and the loss in the catalyst layer due to gas starvation [4]. As a result, the load dynamics should be limited in order to increase the FCS lifetime.

Charge-discharge rate and depth-of-discharge have major effects on the battery lifetime. The battery aging is manifested in a decrease in discharge capacity and an increase in the internal resistance [5,6]. The battery cycle life depends on the operating conditions with few thousand cycles as a typical value.

In comparison to the batteries, supercapacitors have a much longer cycle life (~10^6 cycles). Moreover, they have a much higher specific power, however, with a significantly lower specific energy [7]. As a result, combining the two technologies, battery and supercapacitor, would form an ideal solution to their individual limitations, so that the resulting hybrid ESS would have a high specific power and a high specific energy. Additionally, with the supercapacitor, the battery power can be significantly reduced prolonging its lifetime. The battery in the battery-only ESS is usually oversized in order to fulfill the power and lifetime requirements in hybrid vehicles; therefore, with supercapacitor, the battery size can be significantly reduced. Due to this reduction in battery size, the ESS cost analysis has shown that the hybrid ESS can be more economical than the battery-only ESS [8], and the cost advantage is further increased if the battery aging is taken into account [9].

The power management strategy defines the contribution of the different power sources in fulfilling the power demand while considering the system states. In case of a single energy storage (e.g., battery), which is the most common case in hybrid electric vehicle [10–15], the power management deals with one control variable (e.g., the FCS power or the battery power in case of a fuel cell/battery hybrid) and one controllable state (*i.e.*, the battery state-of-charge). In comparison, adding a supercapacitor to the system implicates an additional degree-of-freedom with additional control variable and state. This additional degree-of-freedom complicates the design and optimization of the power management, where the optimization objectives and the trade-off, if any, between them need to be established and analyzed in order to exploit the power sources while respecting their constraints.

The design of the power management strategy of fuel cell/battery/supercapacitor hybrid systems for vehicular applications has been addressed by many researchers. The proposed strategies can be classified into two categories: off-line optimal strategies and real-time strategies. Dynamic Programming [16] and convex optimization [9] have been used to get the off-line optimal strategy. However, the off-line optimal strategy cannot be used in real-time because it requires a priori knowledge of the driving cycle and, therefore, the design of a real-time strategy is inevitable. Many real-time power management designs have been also proposed. As examples, they are proportional-integral control [8,17], fuzzy logic control [18,19], rule-based control [20], wavelet transform combined with fuzzy logic control [21], sliding mode control [22], and model predictive control [23].

The foregoing papers that deal with the design of real-time power management strategies for fuel cell/battery/supercapacitor hybrids aimed at qualitatively answering the question: does the proposed strategy work? Other interesting questions remained unaddressed in a systematic quantitative manner. For examples, can the strategy be optimized? What are the relevant optimization objective functions? How to resolve any trade-off between the objective functions? The contribution of this paper is the introduction of a new formulation for the optimization of power management strategy that takes into account hydrogen consumption, battery loading, and vehicle acceleration performance in a framework of multi-objective optimization. A genetic algorithm and Pareto front analysis are used to solve the optimization problem. The second contribution of the paper is the introduction of a new proportional-integral controller-based strategy, where the advantages of the proposed strategy in comparison to similar strategies in literature are analyzed. The power management strategy is designed for and validated on a small-scale test bench. The test bench components are first characterized and the resulting models are then used in the optimization process.

A transit bus is considered as an application of the fuel cell/battery/supercapacitor hybrid power source. Section 2 introduces a model of the vehicle that enables the calculation of the power demand necessary to meet a standard driving cycle. The calculated power demand is scaled down to fit our test bench. Models of test bench components are introduced in Section 3. Section 4 introduces the design and optimization of the power management strategy. Experimental evaluation of the optimized strategy is presented in Section 5.

2. Vehicle Model

A schematic of the fuel cell/battery/supercapacitor vehicle is shown in Figure 1. The battery is directly connected to the DC bus, whereas the FCS is coupled to the bus via a unidirectional DC/DC converter that enables the control of the FCS output power. A bidirectional DC/DC converter in front of the supercapacitor provides isolation between the supercapacitor and the battery that operates on different voltage level and enables the control of the supercapacitor power. Its bidirectional operation enables discharging and charging of the supercapacitor. The DC bus feeds the induction electric motor through an inverter. The motor shaft is coupled to the wheels through a single-speed transmission line that includes the reduction gearbox.

The topology shown in Figure 1 is the typical one used for transit buses in literature [8,9,18], due to its advantages over other possible alternative topologies. In this topology, the DC bus voltage is the same as the battery voltage, so that no direct bus voltage regulation exists. A bidirectional DC/DC converter

can be placed between the battery and the DC bus enabling the DC bus voltage regulation, which is beneficial in order to get the full power capability of the traction motors all the time; however, this comes at the expense of additional hydrogen consumption due to the power losses in the converter. Moreover, in comparison to fuel cell/battery hybrid systems, the supercapacitor helps reduce the power burden on the battery by supplying most of the transient power demands and, therefore, the battery voltage does not change significantly. Another alternative topology is to place the bidirectional converter in front of the battery, rather than the supercapacitor. In this case, the bus voltage is determined by the supercapacitor, which exhibits strong voltage variations due to its low energy content (in comparison to the battery) and the high sensitivity of supercapacitor voltage to its charge level.

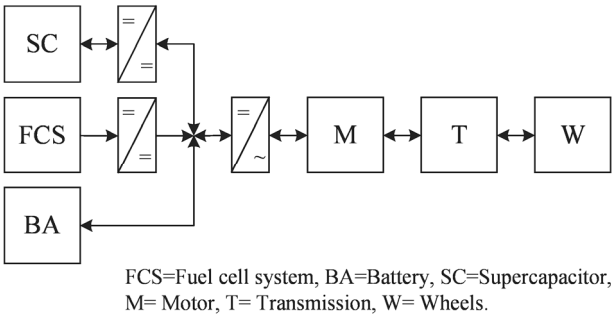

Figure 1. Schematic of fuel cell/battery/supercapacitor hybrid drive train.

The first objective of the vehicle model is to calculate the electric power required by the hybrid power source to meet a given speed profile, $v(t)$. The modeling approach used here is a combination of forward and backward calculations similar to the one used in ADVISOR [24]. The backward calculation path takes the required vehicle speed and calculates the required power at the DC bus. However, if the required power cannot be met by the power source and/or the electric motor, the forward calculation path calculates the achievable speed.

The traction force, F_t, required at the wheels for a given speed is the sum of four forces: the acceleration force, the force required to overcome the aerodynamic drag, the force required to overcome the rolling friction with the road surface, and the gravity force acting on the vehicle when driving on non-horizontal roads (*i.e.*, up or downhill) [25]:

$$F_t = (m + \frac{\Theta_w}{r^2})\frac{dv}{dt} + \frac{1}{2}\rho C_d A_f v^2 + mg\, C_r \cos(\alpha) + mg \sin(\alpha) \quad (1)$$

where m (=15,000 kg) is the vehicle gross mass, Θ_w (=20.5 kg·m^2) is the wheels inertia, r (=0.48 m) is the wheel radius, ρ (=1.2 kg/m^3) is the air density, C_d (=0.79) is the aerodynamic drag coefficient, A_f (=7.86 m^2) is the vehicle frontal area, g (=9.8 m/s^2) is the acceleration of gravity, C_r (=0.009) is the friction coefficient and α is the road angle which is set to zero for the evaluation driving cycle. The Citaro FuelCell Hybrid transit bus from Mercedes Benz [26] is used as a reference for the vehicle parameters.

Given the traction force, the required torque at the wheels and the wheels rotational speed are then obtained. The transmission line is modeled by its efficiency and gear ratio. A single-speed transmission is used with a constant efficiency of 0.95 and a gear ratio of 22.63. The motor is modeled by its efficiency map that defines its efficiency as a function of its torque and rotational speed. The vehicle is driven by

two motors mounted on the rear axle, each motor has a maximum output power of 120 kW, a maximum rotational speed of 11,000 rpm and a maximum torque of 465 N·m. In the braking phases, a maximum of 60% of the braking torque is assumed available for recuperation, whereas the rest is lost in the mechanical brakes. A continuous constant power of 10 kW is assumed to feed the vehicle accessories (e.g., air conditioning, cooling fans, power steering…*etc.*). As a result of the vehicle model, the power demand, P_{dem}, required at the DC bus is calculated as the sum of the traction motor power and the power required by the vehicle accessories. This total power should be met by the three power sources:

$$P_{dem} = P_{fcdc} + P_b + P_{scdc} \quad (2)$$

where P_{fcdc} is the output power of the FCS DC/DC converter (P_{fc} is the FCS output power), P_b is the battery power, and P_{scdc} is the output power of the supercapacitor DC/DC converter (P_{sc} is the supercapacitor power).

Manhattan driving cycle (Figure 2) is used for evaluating the performance of the power management strategy. The corresponding power demand calculated by the vehicle model is downscaled to fit the test bench introduced in the next section. This cycle was developed based on actual transit bus operation in Manhattan [24,27], and it is widely used in literature for the performance evaluation of fuel cell-based transit buses [8,13]. The driving cycle significantly affects the optimization of powertrain size [28] and power management. The sensitivity of driving cycle on the power management optimization, which is the focus of this study, will be discussed in Section 6.

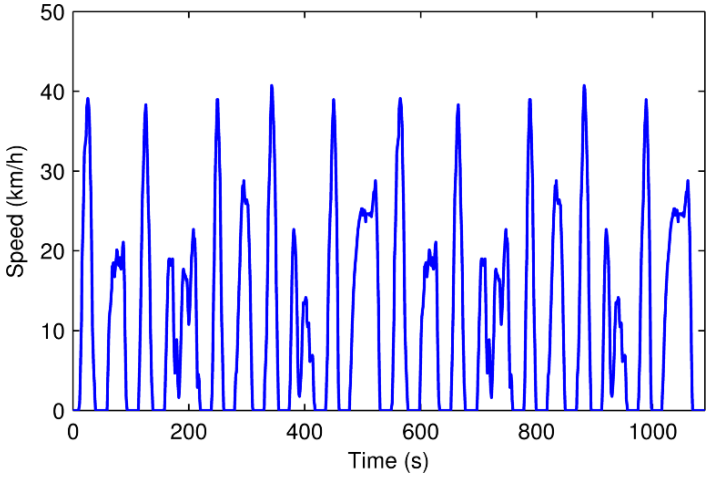

Figure 2. Speed profile of Manhattan driving cycle.

3. Hardware-in-the-Loop Test Bench

The experimental test bench (Figure 3) is composed of a FCS, lithium-polymer battery, supercapacitor, unidirectional DC/DC converter for the FCS, and a bidirectional one for the supercapacitor. The two-quadrant programmable load enables both power sinking as well power sourcing corresponding to the motoring and regenerative braking of the real vehicle. The whole test bench is controlled and monitored in real-time by an xPC-Target computer equipped with fast and high-resolution (16-bit) input/output cards with a sample time of 10 ms. The target application, which includes the power management strategy, is programmed in Simulink environment on a host computer. The communication between the target computer and the host computer serves to download the compiled application to the

target computer and to transfer the collected data from the target to the host computer for evaluation. Table 1 lists the specifications of the test bench components.

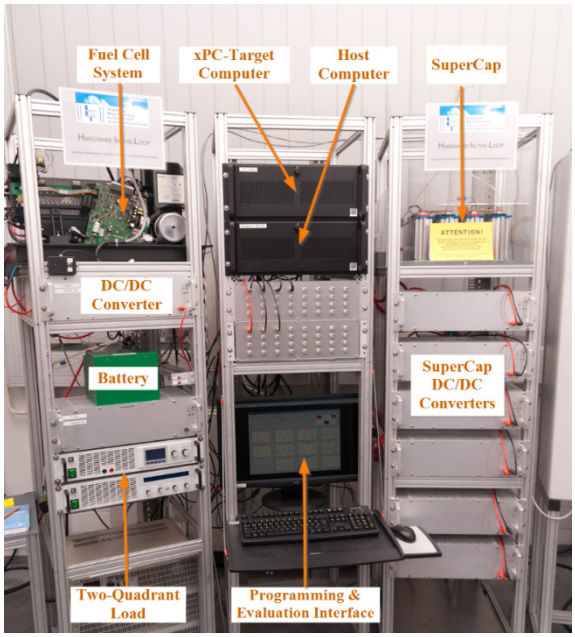

Figure 3. Photograph of the Hardware-in-the-Loop test bench.

Table 1. Specifications of the test bench.

Parameter	Value
Fuel cell system	
PEM stack	47 cells
Rated power	1.2 kW
Output voltage	22–43 V (26 V rated)
Battery	
No. cells	10
Capacity	30 Ah
Rated voltage	37 V
Current (max./min./rated)	(110/−45/30) A
Supercapacitor	
No. modules	3 (each with 6 cells)
Module capacitance	500 F
Rated Voltage	48 V
Current (max./min./rated)	(1900/−1900/100) A
DC/DC converter	
Input voltage	25–47 V (36 V rated)
Output voltage	25–50 V (50 V rated)
Maximum output current	25 A
Load	
Sink ratings	80 V/200 A/2400 W
Source ratings	80 V/50 A/1500 W

The ratings of the DC/DC converter in Table 1 correspond to the unidirectional FCS converter. Four units of this converter are used for the supercapacitor. Voltage and Hall-effect current sensors, with a maximum error of 1%, are installed at the output of each test bench component.

3.1. Fuel Cell System

A 1.2 kW, 26 V FCS from Ballard is used in the test bench. The FCS and its unidirectional DC/DC converter are modeled by their steady state efficiencies shown in Figure 4b, which shows the overall efficiency of the two components, as well. The overall efficiency of the FCS and its DC/DC converter is defined as the ratio of the converter output power, P_{fcdc}, to the hydrogen power, where the hydrogen power is the product of hydrogen mass flow rate and hydrogen lower heating value, LHV (=120 kJ/g). The hydrogen flow rate is modeled by a second-order polynomial function of P_{fcdc} (Figure 4a) fitted to experimental data. Quadratic model of the hydrogen consumption rate was used in [9,10,13], and analytically proven valid in [29]. A comparison between the measured overall efficiency and the model efficiency is illustrated in Figure 4b. Due to aging, the FCS has lost its high power capability and, therefore, P_{fcdc} is limited to 700 W.

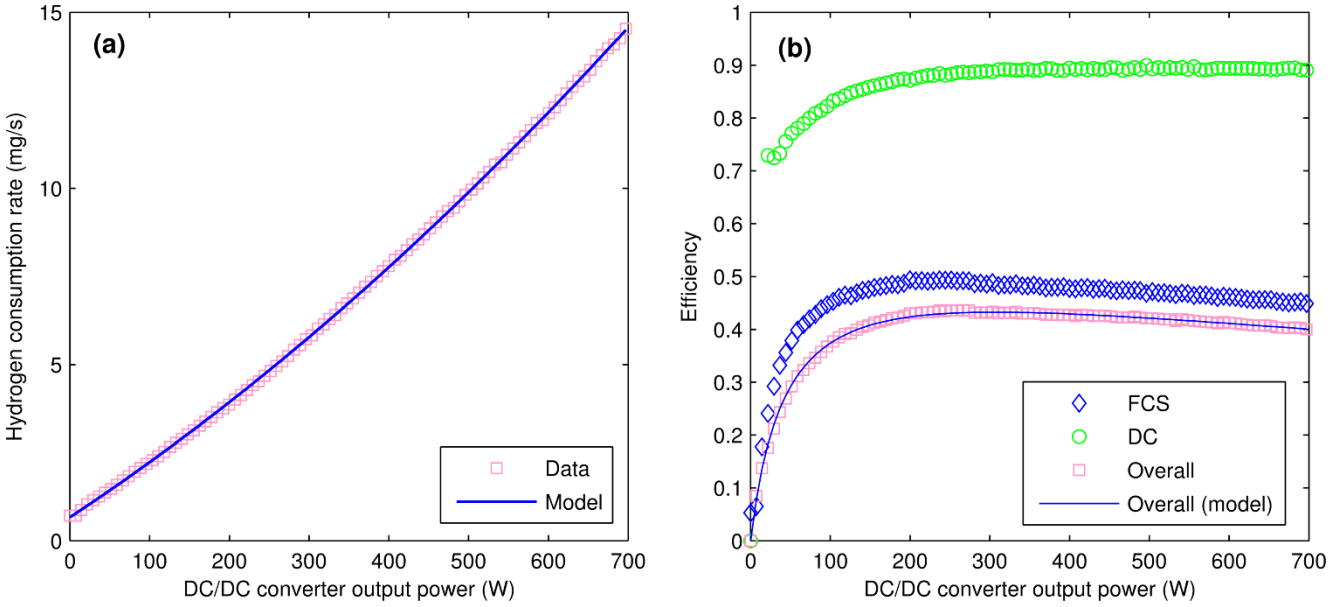

Figure 4. Modeling of the FCS and its DC/DC converter. (**a**) Hydrogen consumption rate; (**b**) Efficiency of FCS and its DC/DC converter.

3.2. Battery

A 30 Ah lithium-polymer battery from Hoppecke is used. It is composed of 10 cells connected in series. The battery is modeled by the internal-resistance model whose equivalent circuit is shown in Figure 5a, where OCV is the open circuit voltage of the battery and R is its internal resistance. Two values of R are usually distinguished: one when charging the battery, R_{chg}, and the other when discharging it, R_{dis}. All the model parameters vary with the state-of-charge (SoC) as shown in Figure 5b. The parameters were identified by an HPPC test (Hybrid Pulse Power Characterization) [30].

The battery SoC is considered as a state of the system denoted as x_b and defined as follows:

$$x_b(t) = \frac{Q_b(t)}{Q_{b,\max}} = x_b(0) - \frac{1}{Q_{b,\max}} \int_0^t I_b(\tau) d\tau \tag{3}$$

where Q_b is the remaining charge, $Q_{b,\max}$ is the charge capacity and I_b is the battery current which is considered positive when discharging the battery and negative otherwise. The battery state is calculated experimentally by Ampere-hour counting as expressed in Equation (3).

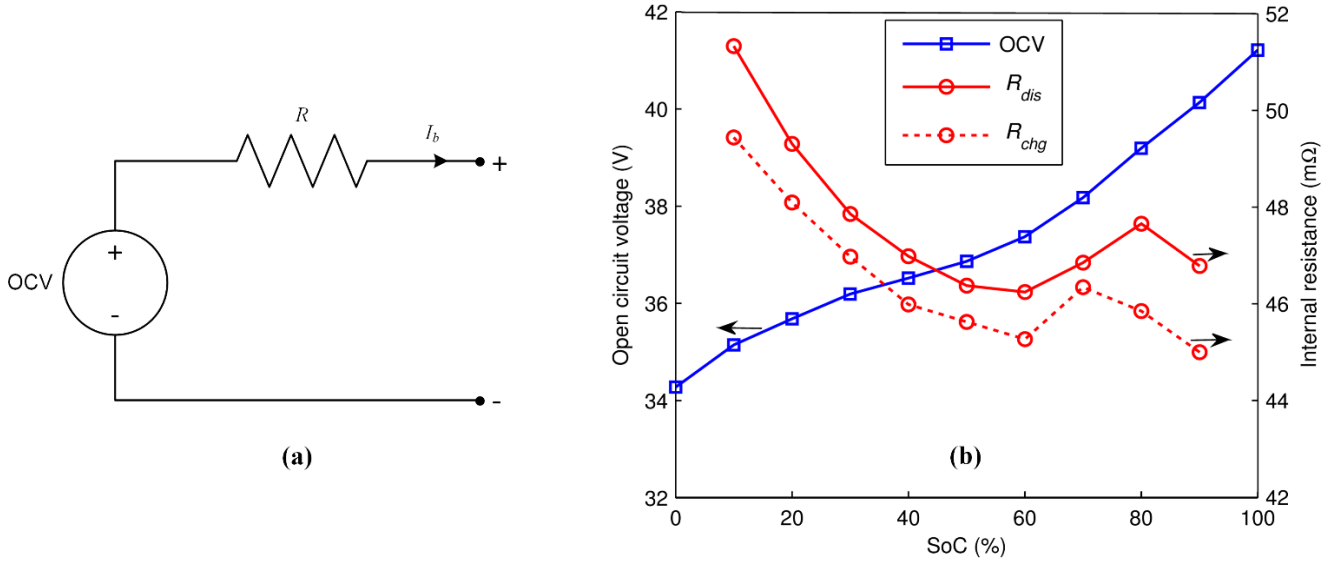

Figure 5. Modeling of the battery by the internal-resistance model. (**a**) Model equivalent circuit; (**b**) Model parameters as a function of SoC.

3.3. Supercapacitor

The supercapacitor bank is composed of three BMOD0500P016B02 6-cell modules from Maxwell Technologies. Each module has a rated capacitance of 500 F, an internal resistance of 2.1 mΩ and a rated voltage of 16 V [31]. These characteristics have been experimentally verified as described in the product datasheet. The supercapacitor bank is modeled by the same model used for the battery (Figure 5a); however, a capacitor is used instated of the voltage source since the open circuit voltage changes linearly with SoC. The state-of-energy (SoE) is commonly used in literature as a state of the supercapacitor, so it will be used here and denoted as x_{sc}. The supercapacitor energy content, E_{sc}, is related to its open circuit voltage V_{sc} by:

$$E_{sc} = 0.5 C V_{sc}^2 \tag{4}$$

where C is the supercapacitor bank capacitance. Therefore, the supercapacitor state is defined as:

$$x_{sc} = \frac{E_{sc}}{E_{sc,\max}} = \left(\frac{V_{sc}}{V_{sc,\max}} \right)^2 \tag{5}$$

where $E_{sc,\max}$ is the supercapacitor energy capacity corresponding to the maximum open circuit voltage of $V_{sc,\max}$ which is equal to the rated voltage. The x_{sc} is limited between 0.25 *(i.e.*, $V_{sc}=V_{sc,\max}/2$) and 0.95 as a safety margin. Hence, the usable energy capacity represents 70% of the theoretical energy capacity.

Experimentally, x_{sc} is estimated by, first, Ampere-hour counting to calculate the SoC and, then, the V_{sc} is estimated and Equation (5) is used.

The bidirectional DC/DC converter of the supercapacitor is formed by four unidirectional converters of the type given in Table 1; two serve to discharge the supercapacitor and the other two to charge it. Figure 6a shows the relation between the power at the supercapacitor side, P_{sc}, and that at the electric bus side, P_{scdc}, for a 37 V voltage at both sides. The difference between them constitutes the power loss in the DC/DC converters. The measured efficiency is shown in Figure 6b, where the efficiency is given as a function of the output power, which refers to the electric bus side when discharging and to the supercapacitor side when charging. The converters used in this study are of relatively low efficiency, whereas an efficiency >95% is currently possible with the state-of-the-art converters designed for automotive applications [32].

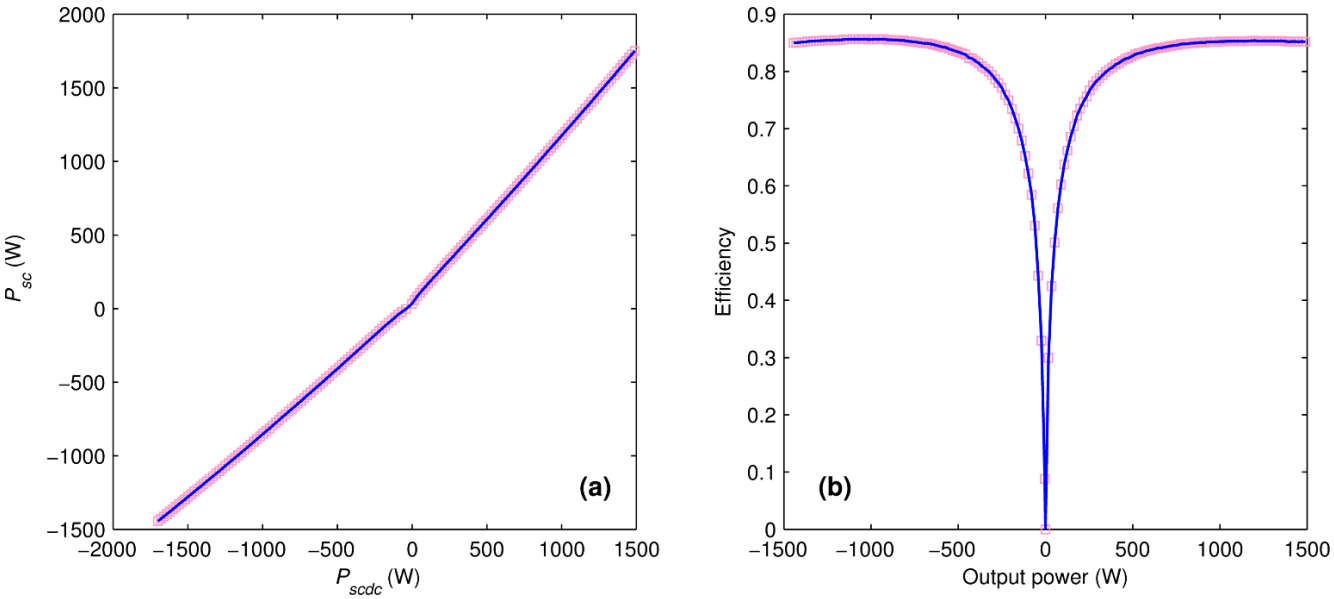

Figure 6. Modeling of the supercapacitor bidirectional DC/DC converter. (**a**) Input-output power relation; (**b**) Efficiency.

In this study, steady state models are used for the three power sources FCS, battery and supercapacitor. Such models are simple enabling a quick simulation and they are characterized by a few parameters that can be easily identified by standard characterization techniques typically used by manufacturers. The quality and sufficiency of such modeling approach can be assessed by comparing the hydrogen consumption and state trajectories between simulation and experiment as will be illustrated in Section 5. However, it is worth noting that there are plenty of more sophisticated, dynamic models in literature. Choosing one modeling approach rather than the others depends very much on the target application of the model. As examples, Pukrushpan *et al.* [33] developed a detailed dynamic model of the FCS taking into account the air and hydrogen supply dynamics. Such dynamic model is necessary if the target of modeling is the control of reactant supply subsystems. An empirical model capable of capturing fuel cell voltage dynamics was used by Boscaino *et al.* [34]. Hu *et al.* [35] compared several equivalent circuit models for Li-ion batteries, where the dynamic behavior of the cell voltage (*i.e.*, voltage relaxation) is represented by RC branches connected in series with the resistance R of Figure 5a. Like batteries, supercapacitors are typically modeled by equivalent circuits. Devillers *et al.* [36] reviewed three equivalent circuit

supercapacitor models including the steady state model used in this study. The supercapacitor voltage dynamics is represented by RC branches and an inductance.

3.4. DC/DC Converters

The DC/DC converters are responsible for the realization of power management strategy. The converter in front of the FCS controls the FCS contribution in meeting the demand at each time instant, whereas the supercapacitor converters control the supercapacitor contribution. The battery contribution is then determined by the power balance. The same converter given in Table 1 is used for the FCS and the supercapacitor, however, with one unit for the FCS and four units for the supercapacitor.

The converters are of buck-boost topology, so that the output voltage can be smaller or higher than the input voltage. They are equipped by two control inputs: one to set the reference output voltage, and one to limit the output current. The reference output voltage can be varied between 25 V and 50 V, and the output current can be limited to any value between 0 and 25 A. The control of the output power is achieved as follows for the FCS converter for example. For the FCS converter, the output voltage is the DC bus voltage that is set by the battery, with about 37 V as a nominal value. In order to set the FCS converter output power to P_{fcdc}, the bus voltage, V_{bus}, is measured and the required output current, $I_{fcdc} = P_{fcdc}/V_{bus}$, is then calculated. The reference voltage of the converter is set always to the maximum value of 50 V. Since the actual output voltage is smaller than the reference, the converter operates in the current-limited mode, so that the output current will be the maximum possible value permitted by the current limitation. So, I_{fcdc} is implemented by the converter if I_{fcdc} is used as a current limitation. The same method is used to control the supercapacitor converters.

3.5. Power Sources Sizing

The sizing procedure of different test bench components is a combination of downscaling of actual sizes in actual transit buses taken from literature and the availability of certain components in the lab. In [37], the topology used for a transit bus consisted of a 120 kW FCS, a 13 kWh lithium-ion battery, and a 0.97 kWh supercapacitor. The FCS power is limited in the test bench to 700 W, therefore, the power demand calculated for the actual vehicle in Section 2 is multiplied by a scaling factor of 0.006 (≈700 W/120 kW) when it is applied to the test bench. The FCS voltage range fits within the DC/DC converter input voltage limits (see Table 1).

The battery and supercapacitor are sized according to their voltage (*i.e.*, number of cells in series) and energy (*i.e.*, capacity of battery and capacitance of supercapacitor). The battery voltage is the same as the DC bus voltage, which should fit the converters voltage ratings. A 10-cell lithium-ion battery is then used with a nominal voltage of 37 V (3.7 V for one battery cell). The supercapacitor cell is operated within the voltage range 1.35–2.7 V, so with 18 cells in series the voltage range is about 24–48 V, which fits as well the used DC/DC converters.

Having set up the required number of cells of battery and supercapacitor, their energy content is still to be chosen. The required energy can be obtained from the energy used in the actual vehicle multiplied by the scaling factor of 0.006. The required test bench battery energy is then 78 Wh (corresponding to a capacity of 2.1 Ah), and 5.8 Wh (corresponding to 320 F cell capacitance) for the supercapacitor. In comparison, the battery used in the test bench has a capacity of 30 Ah, and the supercapacitor cell used

has a capacitance of 3000 F (500 F for a module of six cells in series). Therefore, both energy storages are actually oversized in the test bench by a factor of about 15 for the battery and a factor of about 10 for the supercapacitor. Oversizing the battery capacity implies that the battery SoC swing in the test bench will be smaller than that exhibited by the vehicle battery. However, the operating SoC range is already small in the actual vehicle [18,37] since the battery energy is big and it takes only small part of the transient demands (*i.e.*, most of the transient demand is assigned to the supercapacitor) and, therefore, the SoC range is not a limiting factor for the power management strategy design. As a result, oversizing the battery in the test bench has no major implications that need to be considered. In contrast, the supercapacitor energy content in the actual vehicle imposes a constraint on the power management strategy since the supercapacitor may get depleted during extended acceleration phases. So, in order to mimic the conditions in the actual vehicle, only part of the available supercapacitor energy at the test bench is used. The nominal supercapacitor SoE will be 0.6, and the lower SoE limit is 0.53. A reduction of supercapacitor SoE of 0.07 in the test bench would correspond to a reduction of 0.7 in the vehicle representing a depletion of the vehicle supercapacitor (from Section 3.3, the usable energy is 70% of the installed energy).

4. Power Management Strategy

The triple hybrid is a multiple-input-multiple-output system (MIMO), with P_{fcdc}, P_b and P_{scdc} as inputs (*i.e.*, manipulated variables), and x_b and x_{sc} as outputs (*i.e.*, controlled variables). Two strategies (Figure 7) are introduced and compared. The first strategy, S1, (Figure 7a) is used as a benchmark to illustrate the advantages of the second strategy, S2, (Figure 7b). Both strategies use the battery to regulate the supercapacitor state through a proportional controller (P), whereas the FCS is used to regulate the battery state with the help of a proportional-integral controller (PI). The logic behind such control structure is the following: the supercapacitor is supposed to take care of the peak power demands and it has relatively low energy content and, therefore, its state will change fast. As a result, it requires a fast power source to control its state, which is fulfilled by the battery. In contrast, the battery is responsible for smaller fractions of the transient demand and it has larger energy content and, therefore, its state changes slower with time. As a result, the control of battery state can be achieved by a slow system like FCS.

4.1. Strategy S1

For S1, a PI controller is used to control the battery state around the constant reference $x_{b,ref}$ of 0.6, as give in Equation (6). The output of the controller, u_{fc}, is then fed into a saturation block that limits the control variable between 0 and 700 W. The rate limiter limits the ramp rate of the control variable to ±10 W/s. The output of the rate limiter is used as a reference power for the FCS DC/DC converter. The proportional controller (Equation (7)) controls the supercapacitor state around a constant reference $x_{sc,ref}$ of 0.6, where the battery power P_b equals the output of the controller, u_b. Then the difference $P_{dem} - P_{fcdc} - P_b$ constitutes the reference power for the supercapacitor DC/DC converter:

$$u_{fc}(t) = K_{p,b}\left(x_{b,ref} - x_b(t)\right) + K_{i,b}\int_0^t \left(x_{b,ref} - x_b(\tau)\right)d\tau \quad (6)$$

$$u_b(t) = K_{p,sc}\left(x_{sc,ref} - x_{sc}(t)\right) \tag{7}$$

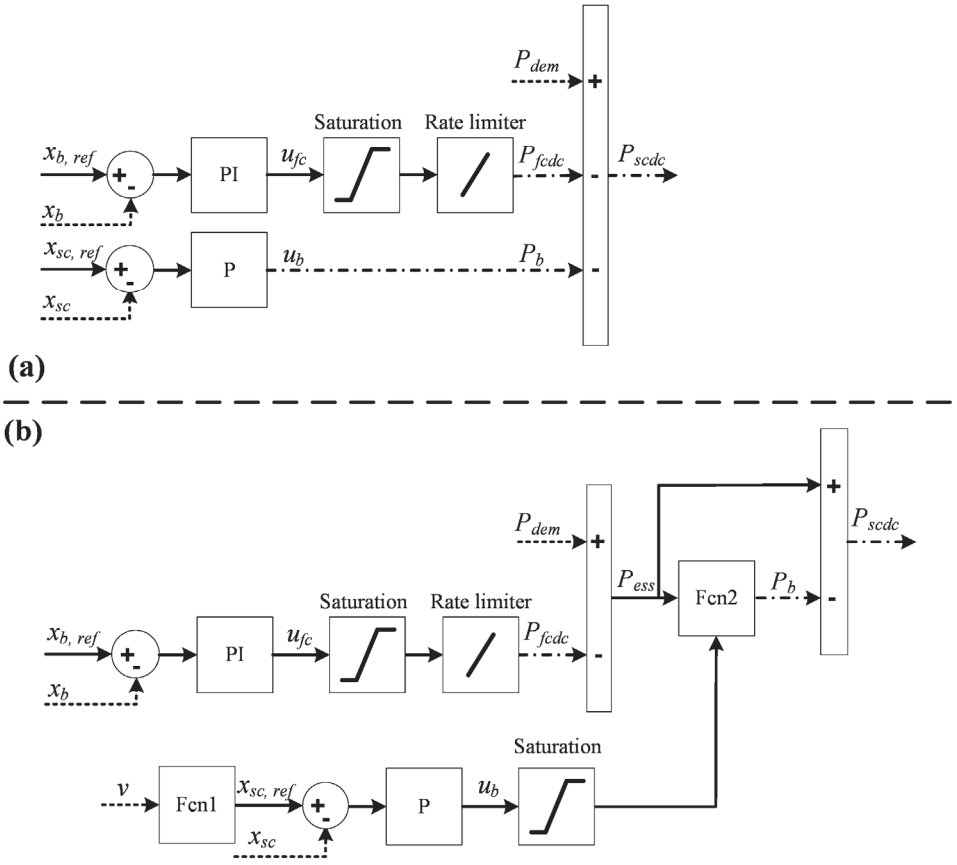

Figure 7. Schematic of the two power management strategies. (**a**) S1; (**b**) S2. The inputs represented by dotted arrows and the outputs by dash-dot arrows.

4.2. Strategy S2

The control loop of x_b in S2 is the same as S1, whereas the control loop of x_{sc} is different. The reference supercapacitor state in S2 is made variable proportional to the vehicle speed squared as expressed in Equation (8), where v_{max} is the vehicle maximum speed of 80 km/h, and $K_{ref,sc}$ is the proportional factor. Making the supercapacitor SoE variable was devised in [38] as a method to optimally exploit the energy stored in the supercapacitor. It is based on the idea that when the vehicle speed increases, its kinetic energy increases in proportion to the square of the speed and, therefore, the amount of regenerative braking energy expected in future also increases. However, since the amount of recuperated energy depends on the way the vehicle decelerates, the proportionality factor $K_{ref,sc}$ is used as a tuning factor. Equation (8) is represented in Figure 7b by the block named Fcn1. u_b in S2 represents the ratio of P_b to the power required by the hybrid energy storage system (*i.e.*, battery and supercapacitor), P_{ess}, which is the difference P_{dem}-P_{fcdc}. In other terms, u_b in S2 represents the battery contribution in fulfilling P_{ess} and, therefore, it is limited between −1 and +1. The battery power, P_b, is then calculated as given in Equation (9), which is represented in Figure 7b by the block named Fcn2. If u_b is positive (*i.e.*, x_{sc} is below the reference and the supercapacitor needs to be charged), the battery assists the supercapacitor in meeting the demand P_{ess} if this demand is positive; otherwise, the battery contribution is set to zero if the demand is negative

to allow charging the supercapacitor with the maximum rate. On the other hand, if u_b is negative (*i.e.*, x_{sc} is above the reference and the supercapacitor needs to be discharged), the battery assists the supercapacitor in meeting the demand P_{ess} if the demand is negative; otherwise, the battery contribution is set to zero if the demand is positive to allow discharging the supercapacitor with the maximum rate:

$$x_{sc,ref}(t) = 0.6 - K_{ref,sc}\left(\frac{v(t)}{v_{\max}}\right)^2 \tag{8}$$

$$P_b(t) = \begin{cases} +u_b(t)P_{ess}(t) & u_b(t) > 0 \;\&\; P_{ess}(t) > 0 \\ -u_b(t)P_{ess}(t) & u_b(t) < 0 \;\&\; P_{ess}(t) < 0 \\ 0 & Otherwise \end{cases} \tag{9}$$

The goal of formulating the control loop of supercapacitor state in S2 as described above is to avoid the charge exchange between the battery and supercapacitor. According to Equation (9) and to the saturation of u_b between −1 and +1, P_b lies always between zero and P_{ess}, and P_{scdc} is the difference P_{ess}−P_b and, therefore, P_b and P_{scdc} have always the same sign. In contrast, it is possible to have such charge exchange in S1, for example, if $x_{sc} < x_{sc,ref}$ (*i.e.*, $P_b > 0$) and P_{dem}–$P_{fcdc} < 0$.

In summary, S2 has three main features that distinguish it from S1. First, in S2, the supercapacitor reference state is made variable with the speed, whereas this reference is constant in S1. Second, the charge exchange between the battery and supercapacitor is excluded in S2, whereas such exchange is possible in S1. Third, P_b in S2 takes into account, in addition to the difference $x_{sc,ref}$−x_{sc}, P_{ess} (and, hence, P_{dem}), whereas in S1, P_b considers only the difference $x_{sc,ref}$−x_{sc}.

The strategy S1 used here is similar to the strategy used in [8,17], so it is used as a benchmark for the evaluation of the advantages of S2. In [17], the battery and supercapacitor voltages, rather than their states, are used as controlled variables and proportional controllers are used for the two control loops. A proportional controller is used in [8], as well, to regulate the supercapacitor SoE around its variable reference. In both studies, the charge exchange between the battery and the supercapacitor was possible.

4.3. Optimization

The design of the power management strategy is reduced to the selection of controllers parameters, $K_{p,sc}$, $K_{p,b}$ and $K_{i,b}$ for S1, and $K_{p,sc}$, $K_{p,b}$ and $K_{i,b}$ in addition to $K_{ref,sc}$ for S2. The selection criteria are as follows: (1) minimizing the hydrogen consumption; (2) the supercapacitor is responsible for most of the transient power so that the battery contribution is minimized.

The first design objective function, J_1, is the total hydrogen consumption over the driving cycle (where t_f is the cycle duration), whereas the second objective, J_2, is the average absolute power of the battery:

$$\begin{aligned} J_1 &= \int_0^{t_f} \dot{m}_h(t)dt \\ J_2 &= \frac{1}{t_f}\int_0^{t_f} |\, P_b(t)\,|\, dt \end{aligned} \tag{10}$$

Minimizing the two objectives leads to a multi-objective optimization [39] (pp. 16–44), [40]. In case of a single objective, one attempts to obtain the best solution, which is superior to all other alternatives.

In the case of multiple objectives, there does not necessarily exist a solution that is best with respect to all objectives. A solution may be best in one objective but worst in other objectives. Therefore, for the multiple-objective case, there usually exist a set of solutions that represent a trade-off between the objectives and cannot simply be compared with each other. For such solutions, called non-dominated solutions or Pareto front, no improvement in any objective function is possible without sacrificing at least one of the other objective functions. The multi-objective optimization algorithms use the concept of domination, so that two solutions are compared based on whether one dominates the other or not. A solution X_1 is said to dominate the other solution X_2, if the following two conditions are true:

(1) The solution X_1 is no worse than X_2 in all the objectives.
(2) The solution X_1 is strictly better than X_2 in at least one objective.

If any of the above conditions is violated, the solution X_1 does not dominate the solution X_2. The solution is called non-dominated and, hence, belongs to the Pareto front if and only if there does not exist another solution that dominates it.

One of the most popular and widely used algorithms for solving multi-objective optimization problems is Non-dominated Sorting Genetic Algorithm II (NSGA-II) [39] (pp. 233–241), [41], which makes use of a genetic algorithm for calculating the Pareto front. A genetic algorithm is a method for solving optimization problems based on a natural selection process that mimics biological evolution. The algorithm repeatedly modifies a population of individual solutions. At each step, the algorithm randomly selects individuals from the current population and uses them as parents to produce the children for the next generation. Over successive generations, the population evolves toward an optimal solution. The genetic algorithm can be used to solve problems that are not well suited for standard optimization algorithms, including problems in which the objective function is discontinuous, non-differentiable, stochastic, or highly nonlinear. NSGA-II is already implemented as part of Matlab global optimization toolbox [42]. It is used in this study, where the two metrics J_1 and J_2 of Equation (10) constitute the two objective functions, and the strategies parameters are the optimization variables (*i.e.*, decision variables), with a population size of 100 and with Manhattan as a driving cycle.

The optimization problem is constrained by upper and lower bounds on the optimization variables. The limits of the optimization variables are set as follows. The integral parameter $K_{i,b}$ is set to a constant of 100 for the two strategies. The role of this parameter is to guarantee a zero steady state error in the battery state, which is not a part of optimization problem. $K_{p,b}$ is limited between 0 and 10^6 for the two strategies, whereas $K_{p,sc}$ is limited between 0 and 10^6 for S1 and between 0 and 10^3 for S2. $K_{ref,sc}$ is limited for S2 between 0 and 0.1. The parameters ranges are chosen so wide in order to explore wide ranges of the objective functions. However, if a certain range is of interest, then the ranges can be narrowed correspondingly.

It should be noted that evaluating the objective functions requires the system states at the beginning of the driving cycle to be the same as the states at the end of the driving cycle (*i.e.*, charge sustaining performance). For a set of optimization variables to be tested by the optimization algorithm, the strategies are simulated over the driving cycle starting from initial states of 0.6 for the battery and the supercapacitor. If the final states are different from the initial states, the initial states are varied and the simulation is repeated until the charge sustenance is achieved [24], where the objective functions are then calculated.

For most cases, the charge sustenance is obtained in the second simulation run if it is initiated by the final states of the first run.

The resulting Pareto fronts of the two strategies, S1 and S2, are shown in Figure 8a. The Pareto solutions indicate that there is a trade-off between the two objective functions. This trade-off is attributed to the fact that increasing the contribution of the battery decreases the contribution of the supercapacitor and, therefore, reduces the losses in the supercapacitor DC/DC converter, which leads to a lower hydrogen consumption. S2 achieves lower hydrogen consumption than S1 at the same battery contribution. This is a direct result of the fact that there is no charge exchange between the battery and the supercapacitor for S2, whereas such exchange exists for S1. Such charge exchange is accompanied by losses in the battery, the supercapacitor and mainly in the supercapacitor DC/DC converter. This becomes clearer if the average absolute supercapacitor contribution, J_3, defined by Equation (11) is considered. The relation between J_3 and J_2 for the two strategies is depicted in Figure 8b for the Pareto solutions of Figure 8a. J_3 decreases linearly with J_2 for S2, whereas the relation is more complex for S1. In summary, for the same J_2, in comparison to S1, S2 achieves a smaller J_3, and this reduction in J_3 causes less energy loss in the supercapacitor DC/DC converter resulting in overall lower hydrogen consumption. The difference between the two strategies is smaller at smaller battery contribution, since at such low battery contribution, the charge exchange between the battery and the supercapacitor in S1 is also smaller. The difference between the two strategies increases with decreasing the efficiency of the supercapacitor DC/DC converter:

$$J_3 = \frac{1}{t_f}\int_0^{t_f} \left| P_{scdc}(t) \right| dt \tag{11}$$

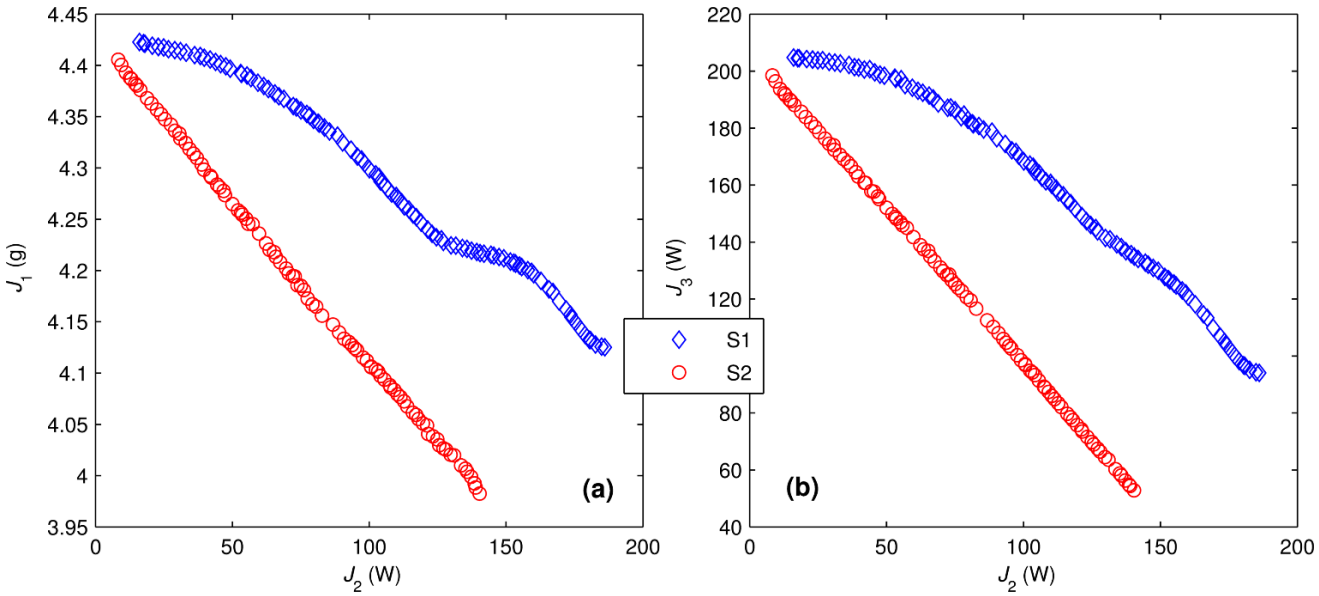

Figure 8. Optimization results of the power management strategies over Manhattan driving cycle. (**a**) Pareto front of J_1 and J_2; (**b**) J_3 *versus* J_2 for the Pareto solutions. The functions J_1, J_2 and J_3 are defined by Equations (10) and (11).

Figure 9 provides more insight into the optimal results for S1, as an example. In order to test the optimality of the resulting Pareto front, the objective functions J_1 and J_2 have been evaluated for random

parameters, $K_{p,b}$ and $K_{p,sc}$, and the results are shown in Figure 9a together with the Pareto front. As shown, NSGA-II results in the best trade-off between the two objectives so that no tested random solution lies below the Pareto front; in other terms, a careless tuning of the parameters may lead to unnecessary and avoidable degradation in one or both of the objective functions. Figure 9b shows the optimal parameters that achieve the Pareto front. The trend of the parameters is so that increasing J_2 increases $K_{p,sc}$ and decreases $K_{p,b}$. Increasing J_2 is achieved by making the battery power more reactive to the variations of supercapacitor SoE (*i.e.*, higher $K_{p,sc}$). Increasing J_2 also increases the operation window of battery SoC, making the required $K_{p,b}$ smaller.

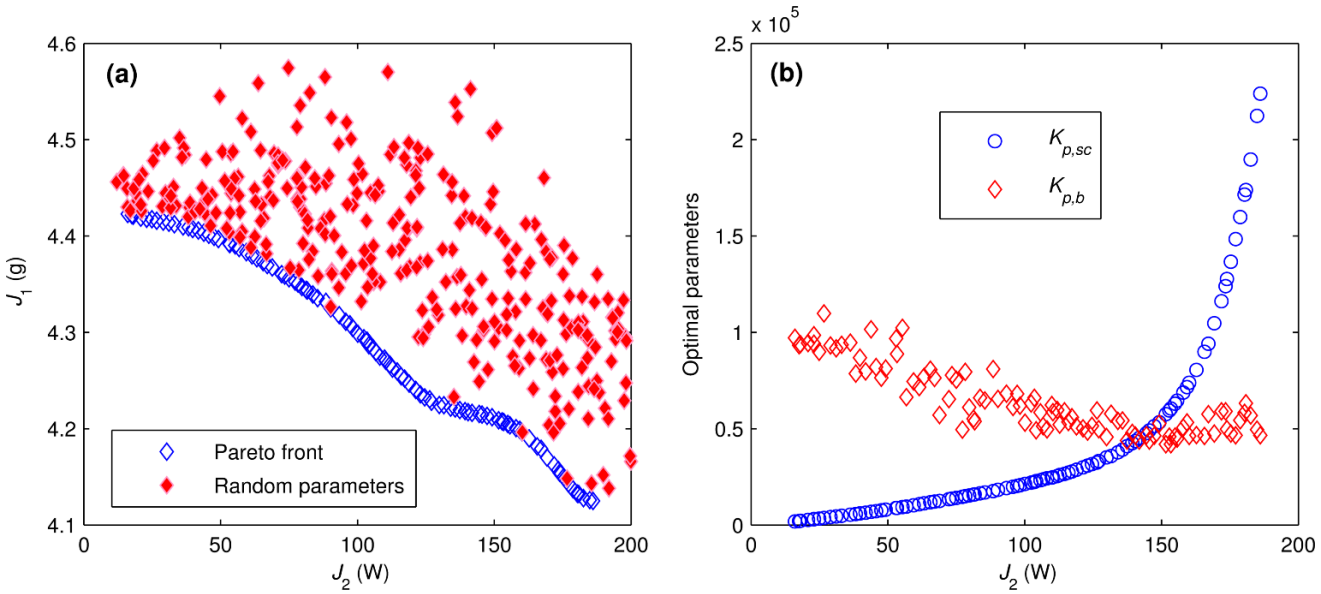

Figure 9. Optimization results of S1. (**a**) Comparison between the Pareto front and the performance of randomly tuned parameters; (**b**) Optimal strategy parameters for the Pareto front.

All the solutions of the Pareto front are mathematically equally optimal. The choice among them requires weighing the relative importance of J_1 and J_2, and testing whether a certain battery contribution (*i.e.*, J_2) is enough to assist the supercapacitor. Here we put a major importance on J_2, so that advantage of using the supercapacitor is fully exploited. Hence, the Pareto solution that achieves the minimum enough battery contribution is considered. To test the sufficiency of a certain J_2, the Pareto solutions are evaluated on a strong acceleration 0–60 km/h shown in Figure 10, where the acceleration starts at time 2 s and takes about 11 s to complete. A speed over 60 km/h is rarely encountered in standard transit bus driving cycles. The Pareto solutions are tested in the direction of increasing J_2, and the minimum that achieves a final x_{sc} larger than 0.53 (starting from 0.6) is considered, where 0.53 is considered as the lower limit for x_{sc} (see Section 3.5).

The above selection procedure is illustrated in Figure 11, which shows the evaluation of strategy S1 over the acceleration phase for three Pareto solutions (corresponding to J_2 = 20, 71 and 120 W). For J_2 of 20 W, the battery contribution is very small at the initial stages of the acceleration, whereas the supercapacitor is strongly loaded, so that the supercapacitor SoE reaches its lower limit of 0.53 before completing the acceleration. After about 8 seconds of acceleration, the battery needs to deliver the required power alone. If the battery is not capable of providing the required power, the acceleration time is prolonged. Therefore, a J_2 of 20 W is considered "insufficient." On the contrary, for J_2 of 120 W, the battery

contribution is relatively high from the beginning of acceleration, so that the supercapacitor is less loaded and its final SoE is 0.55. This case is denoted in Figure 11 as "oversufficient". The value J_2 of 71 W represents the border between the last cases, where the supercapacitor survives the acceleration phase and ends up at its minimum SoE at the end of acceleration. This case is denoted in Figure 11 as "just sufficient," and it is considered as a design point for the strategy S1. In conclusion, the value of J_2 plays a role of a tuning parameter for the strategy, which can be tailored according to the design preferences and system specifications. For example, a small supercapacitor requires higher J_2 (*i.e.*, higher battery contribution), whereas large supercapacitor requires less battery contribution.

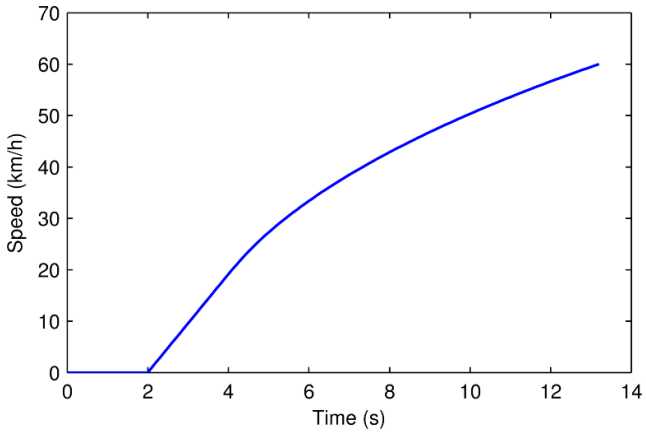

Figure 10. Speed profile during the maximum acceleration 0–60 km/h.

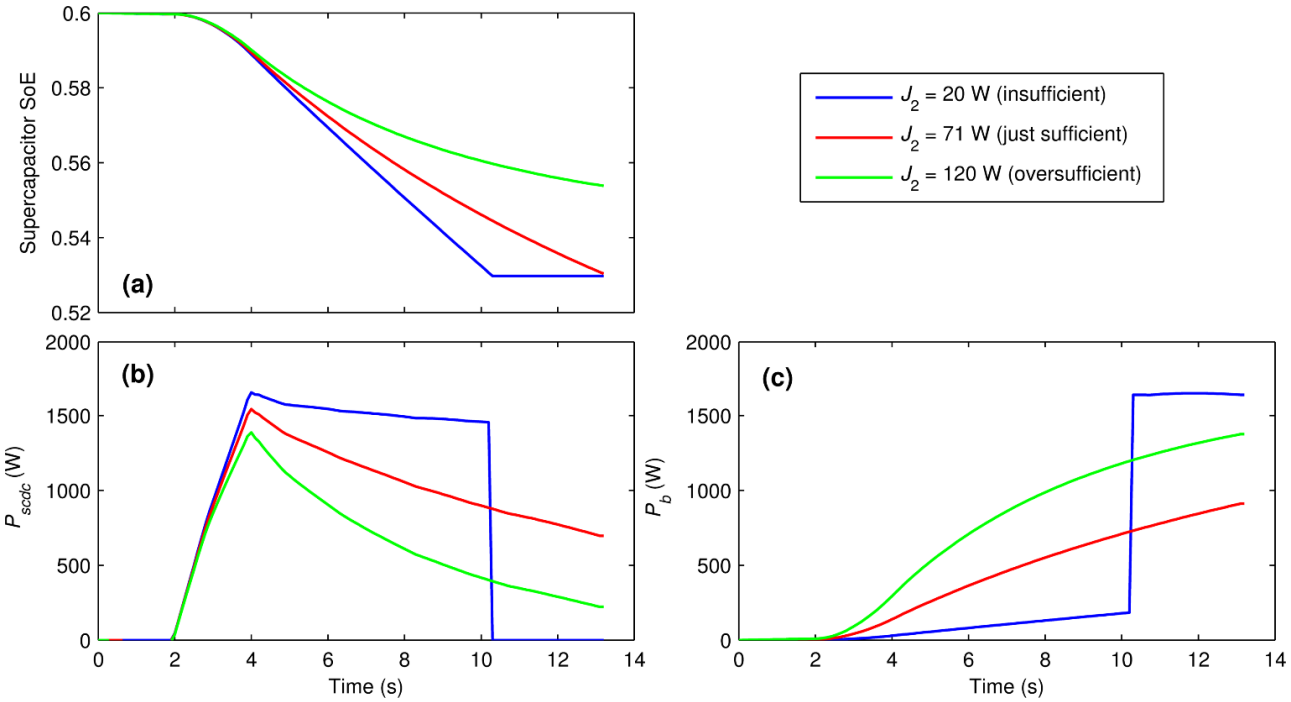

Figure 11. Evaluation of three Pareto solutions with three values of J_2 for the strategy S1. (**a**) Supercapacitor SoE; (**b**) Supercapacitor power; (**c**) Battery power.

As a result of the aforementioned parameters selection procedure, it has been found that the minimum J_2 required is 71 W (corresponding to $K_{p,b} = 6.7 \times 10^4$ and $K_{p,sc} = 1.3 \times 10^4$) for S1, and only 7 W (corresponding to $K_{p,b} = 7.9 \times 10^5$, $K_{p,sc} = 25.8$ and $K_{ref,sc} = 0.092$) for S2. This means that S2 achieves

the same performance during the strong acceleration while having 90% lower battery loading during the normal driving cycles. The two strategies with the chosen parameters are experimentally evaluated in the next section.

5. Experimental Validation

The results of the simulation and optimization are validated in this section. The test bench has been introduced in Section 3, and the power management strategies have been presented and their parameters have been optimized by simulation in Section 4.

As described in Section 4, the parameters of two strategies have been selected among the solutions of the Pareto front based on the acceleration performance. Figure 12 shows the evaluation of the strategies over the acceleration phase. The supercapacitor ends up at a final state of 0.53, which is the value used to select the strategies parameters. The total energy supplied by the battery during the acceleration is the same in both strategies (about 15 Wh). However, The battery power increases faster in S2 at the initial stages of the acceleration (e.g., at time 4 s, the battery power is 220 W for S2 and 130 W for S1), because, as explained in Section 4, the battery power in S2 is also dependent on the power demand, not only the current supercapacitor state. The demand increases fast at the beginning of acceleration, and so does the battery power in S2. In contrast, the battery power in S1 depends solely on the supercapacitor state and, therefore, it increases relatively slowly at the beginning. Since the consumed battery energy is the same in both strategies, the maximum required battery power is smaller for S2 in comparison to S1 (e.g., 915 W for S1 and 743 for S2 at the end of the acceleration).

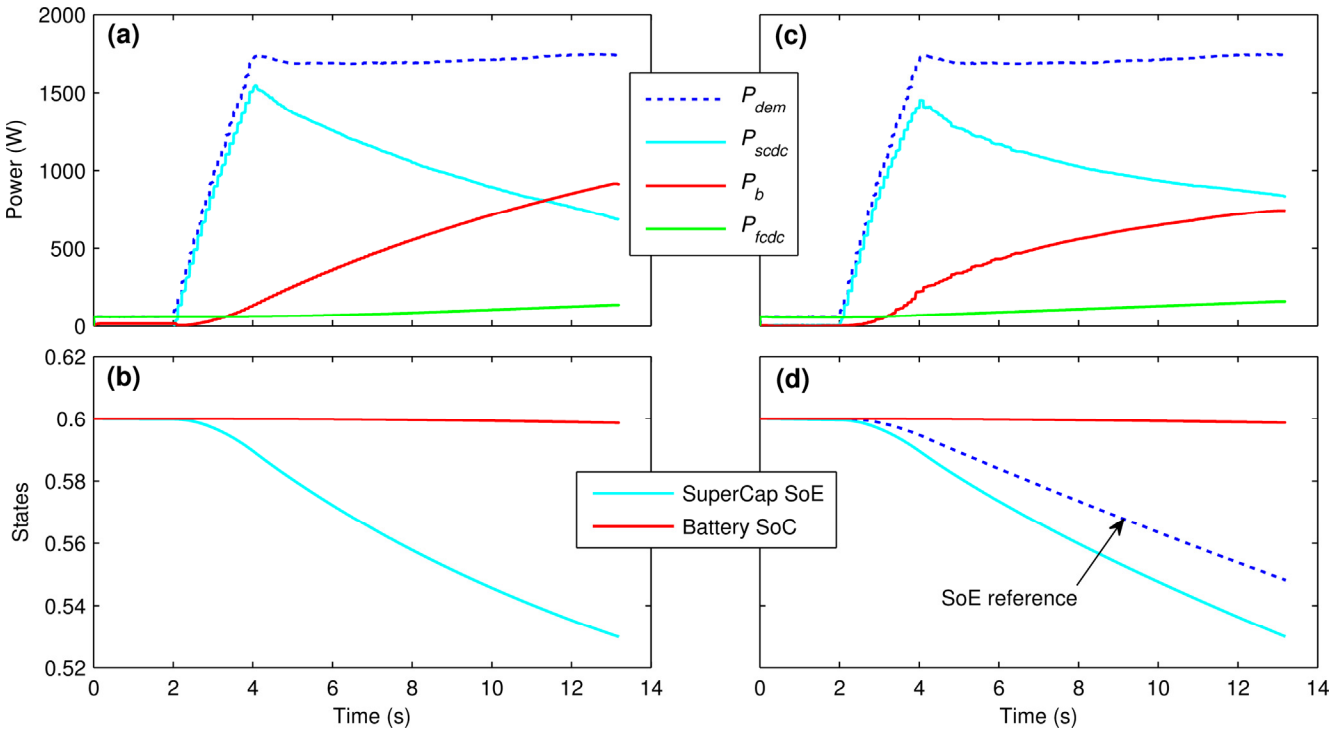

Figure 12. Experimental evaluation of the two strategies, S1 and S2, during the acceleration phase. (**a**) S1 power distribution; (**b**) S1 states trajectories; (**c**) S2 power distribution; (**d**) S2 states trajectories.

In order to experimentally validate the objective functions, J_1 and J_2, the two strategies S1 and S2 are evaluated over Manhattan driving cycle as shown in Figures 13 and 14, respectively, for a charge sustaining performance. The power measurements are obtained from the output currents of the battery, FCS converter and supercapacitor converter multiplied by the DC bus voltage. The states of the battery and supercapacitor are obtained from their current measurements as described in Sections 3.2 and 3.3, respectively. The test bench replicates the simulation results very well as illustrated in the comparison between simulation and experiment in terms of states trajectories. The second observation is that S2 requires negligible battery contribution in comparison to S1. Over the driving cycle, the battery power for S2 is very small; however, this contribution is significant during harsh accelerations as shown in Figure 12. Table 2 quantitatively compares the simulation and experiment in terms of the performance metrics J_1 and J_2.

Table 2. Comparison between simulation and experiment in terms of the performance indices J_1 and J_2. sim. = simulation, exp. = experiment.

Strategy	J_2 (W) (sim./exp.)	J_1 (g) (sim./exp.)
S1	71/73	4.36/4.42
S2	7/8	4.41/4.45

As a result of the experimental evaluation, S2 excels S1 since it achieves a dramatic reduction of the battery loading (about 90% lower in comparison to S1) during normal driving cycles while performing equally well in terms of supercapacitor assistance during strong acceleration phases and in terms of hydrogen consumption (only about 1% higher than S1).

It should be noted that in Figures 12–14, the reference state trajectory is shown only for supercapacitor SoE in S2 because it is variable, whereas the constant battery SoC reference of 0.6 and the constant supercapacitor SoE reference of 0.6 in S1 are not shown. During driving cycle operation, the system is in the transient state where the variable power demand represents a disturbance to the system control and, therefore, the actual state and its reference do not match. On the other hand, if a constant speed is maintained by the vehicle for a sufficiently long time, the system operates in the steady state where the FCS provides the whole demand and the battery and supercapacitor states match their references. This can be also seen from supercapacitor SoE trajectory in Figure 14, where the actual state tends to catch up with the reference when the reference stays constant (*i.e.*, the speed stays constant).

The detailed analysis of the power flow in the triple hybrid system considered is quite complex, where every power source exchanges energy with the other two sources and with the load. However, the main characteristics of the system behavior can be analyzed by grouping two sources and/or considering two sources at a time. Considering the battery/supercapacitor as a hybrid energy storage system, ESS, with a power $P_{ess} = P_{dem} - P_{fcdc}$, three main modes of operation can be recognized during Manhattan driving cycle for both strategies:

(1) $P_{dem} > 0$ and $P_{fcdc} < P_{dem}$ ($P_{ess} > 0$): both FCS and ESS provide the demand.
(2) $P_{dem} > 0$ and $P_{fcdc} > P_{dem}$ ($P_{ess} < 0$): FCS provides the whole demand and charges the ESS.
(3) $P_{dem} < 0$ (*i.e.*, regenerative braking) ($P_{ess} < 0$): both FCS and load charge ESS.

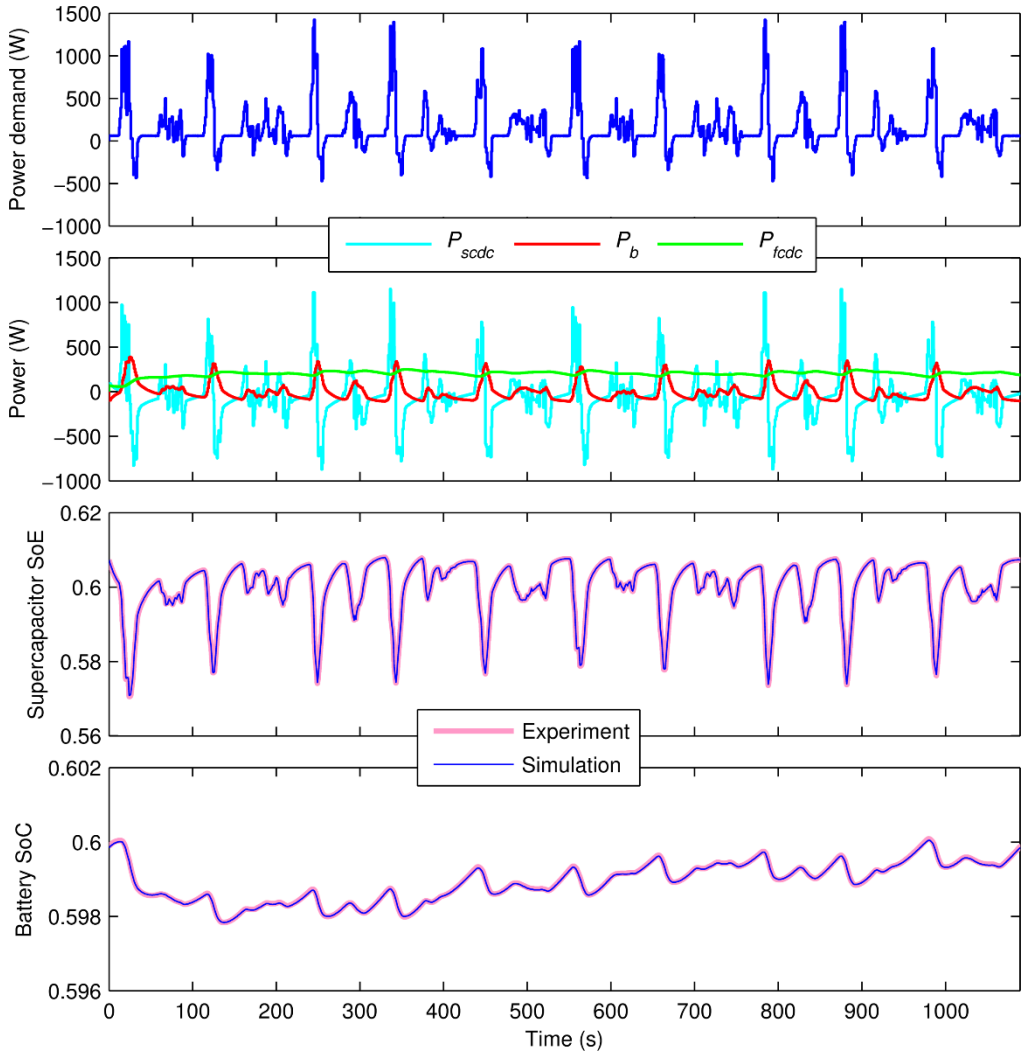

Figure 13. Experimental evaluation of the power management strategy S1 over Manhattan.

The power P_{ess} represents the net power of the hybrid ESS; therefore, the power exchanged between the battery and the supercapacitor does not appear in P_{ess}. Having such power exchange means that one of the two ESS components charges the other. Obtaining information about this power exchange requires looking at the power profile of one ESS component, battery or supercapacitor. The battery power P_b can be divided into two terms: one term represents the contribution of battery to P_{ess} and the other term represents the battery power fed to the supercapacitor. If the second term is positive, the battery is charging the supercapacitor; otherwise, the supercapacitor is charging the battery. Figure 15 illustrates the analysis of battery power over the time 400–600 s of Manhattan for the two strategies.

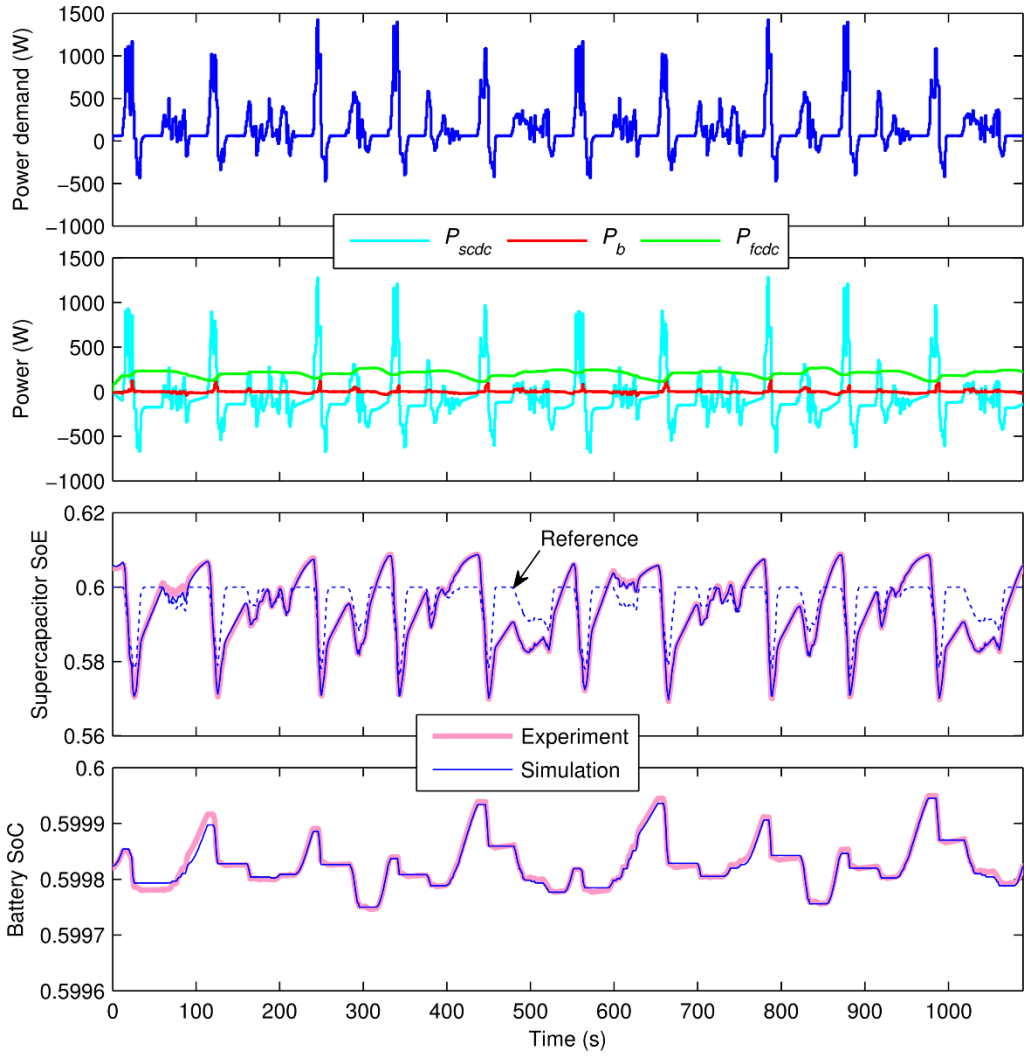

Figure 14. Experimental evaluation of the power management strategy S2 over Manhattan.

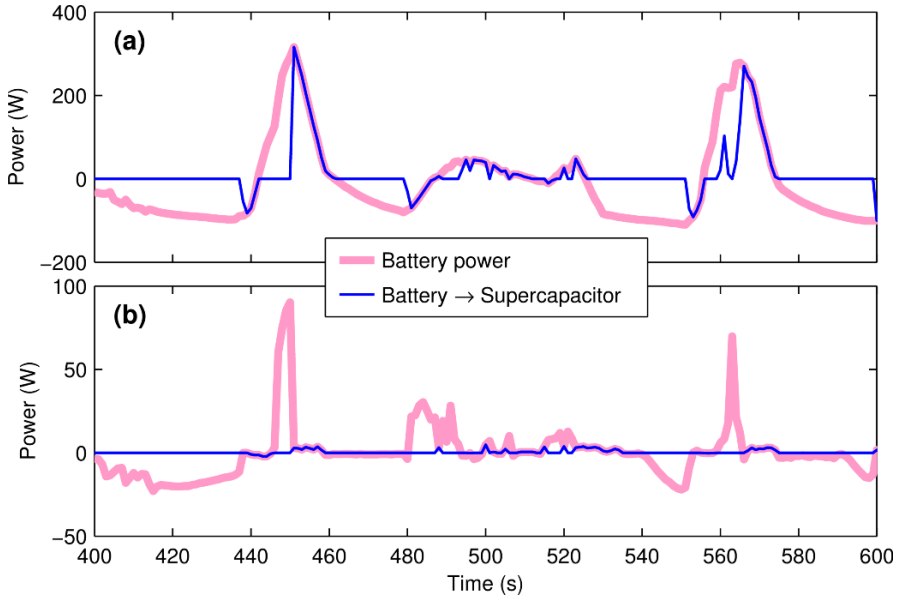

Figure 15. Experimental battery power and its part exchanged with the supercapacitor for (**a**) S1; and (**b**) S2.

The figure shows the total battery power and its part directed to the supercapacitor. The difference between the two curves represents the battery contribution to P_{ess}. For S1 (Figure 15a), a significant part of the battery contribution is due to the power exchange with the supercapacitor, and the power exchange happens in the two directions; *i.e.*, the battery can charge the supercapacitor and the supercapacitor can charge the battery. As stated earlier, S2 is designed so that the power exchange within the hybrid ESS is prevented, which is illustrated in Figure 15b. There are some traces of power exchange (less than 5 W) in Figure 15b due to measurement errors. In summary, for S2, the battery never charges the supercapacitor and the supercapacitor never charges the battery.

6. Further Discussion

The power management strategies have been optimized over Manhattan driving cycle for evaluation purposes. The optimization results may be only quantitatively different if the optimization is done over another driving cycle. The superiority of S2 over S1 in terms of Pareto front and battery contribution remains intact since this superiority results from the strategy design regardless of the driving cycle. However, the optimal performance indices and the optimal strategy parameters may be different, so that the optimal strategy over one driving cycle may not result in an optimal performance over another one. When it comes to the design of a strategy for an actual transit bus, it is recommended, therefore, to include several driving cycles in the optimization problem in order to increase the robustness of the resulting strategy when it is applied to real-world driving conditions. Considering several driving cycles simultaneously can be done by averaging the performance indices across all the driving cycles engaged in the optimization using the same concept used in [10].

As stated in Section 4.1 and shown in Figure 7, the rate of FCS power change is limited to ±10 W/s. The effect of this limitation has been studied by repeating the optimization with a weaker rate limitation of ±100 W/s. It has been found that relaxing the rate limitation has a marginal effect on the optimal Pareto front for the two power management strategies. However, a significant effect has been observed on the size of the dominated space, *i.e.*, the solutions that are dominated by the Pareto front solutions. For example, for S1 and a rate limitation of ±10 W/s, the maximum J_1 at J_2 of 71 W was 4.61 g, about 6% higher than the optimum. In comparison, for a limitation of ±100 W/s, the maximum J_1 was 4.86 g, about 11% higher than the optimum. This observation is attributed to the fact that by relaxing the rate limitation, the FCS power is allowed to span a wider range including the low efficiency regions (very low and very high power), whereas the optimum is to keep the FCS power at its high efficiency region. In our system, the high efficiency FCS operating points coincide with the average power demand of the Manhattan driving cycle. It should be noted that the maximum J_1 at certain J_2 is obtained by repeating the optimization problem while considering the maximization of J_1 instead of its minimization.

One of the advantages of strategy S2 over S1 is the significant reduction in battery loading so that the advantage of using a supercapacitor is better exploited; it is, therefore, worth discussing how this advantage translates into an improvement in battery lifetime. One of the methods used to quantitatively characterize the battery lifetime and aging is the total energy throughput (or equivalently the total Ah-throughput) that the battery can support before the end-of-life, by which the battery capacity fades to 80% of its initial value. The energy throughput (Ah-throughput) is defined as the total energy (charge) that is transferred to and from the battery. Other stress factors such as temperature, depth-of-discharge and charge-discharge

rate may be accounted for as weighting factors when counting the battery throughput [43,44]. A detailed analysis of battery lifetime is beyond the scope of this paper, because the extent of the effect of different stress factors on the battery lifetime depends very much on the battery chemistry, and relevant data for the battery used in this study are not available. However, as a rule of thumb, reducing the average battery power by 90% (as S2 does in comparison to S1 over Manhattan driving cycle) decreases the energy throughput by 90% and, therefore, prolonging the service life of the battery tenfold.

7. Conclusions

This paper was intended to introduce an approach to the design and optimization of the power management strategy of a fuel cell/battery/supercapacitor hybrid system. The strategy was based on two decoupled control loops: one for the state-of-energy of the supercapacitor and the other for the control of the battery state-of-charge. The controller parameters were tuned by a genetic algorithm and Pareto front analysis in a framework of multi-objective optimization, where the hydrogen consumption and the average battery power were used as two objectives to be minimized. By comparing two strategy schemes, two main advantageous features of the power management strategy were identified. First, the charge exchange between the battery and the supercapacitor should be avoided and, second, the battery power should take the power demand into account in addition to the supercapacitor state. These two features resulted in excellent performance in terms of battery loading, hydrogen consumption and acceleration. The optimization results were validated on a small-scale test bench. The simulation results were perfectly reflected on the test bench thanks to the good models of the test bench components.

Acknowledgments

The doctoral fellowship of the corresponding author is granted by the Atomic Energy Commission of Syria (Syria).

Author Contributions

The corresponding author was responsible for the literature review, the design of experiments and the initial writing of the manuscript. The co-authors contributed to the evaluation of the experimental results and reviewing the manuscript before submission.

Conflicts of Interest

The authors declare no conflict of interest.

References

1. Veziroglu, A.; Macario, R. Fuel cell vehicles: State of the art with economic and environmental concerns. *Int. J. Hydrog. Energy* **2011**, *36*, 25–43.
2. Fuel Cell Technology Challenges—US Department of Energy. Available online: http://www.energy.gov (accessed on 10 March 2015).
3. Pei, P.; Chang, Q.; Tang, T. A quick evaluating method for automotive fuel cell lifetime. *Int. J. Hydrog. Energy* **2008**, *33*, 3829–3836.

4. Pei, P.; Chen, H. Main factors affecting the lifetime of Proton Exchange Membrane fuel cells in vehicle applications: A review. *Appl. Energy* **2014**, *125*, 60–75.
5. Broussely, M.; Biensan, P.; Bonhomme, F.; Blanchard, P.; Herreyre, S.; Nechev, K.; Staniewicz, R.J. Main aging mechanisms in Li ion batteries. *J. Power Sources* **2005**, *146*, 90–96.
6. Ecker, M.; Nieto, N.; Käbitz, S.; Schmalstieg, J.; Blanke, H.; Warnecke, A.; Sauer, D.U. Calendar and cycle life study of Li(NiMnCo)O_2-based 18650 lithium-ion batteries. *J. Power Sources* **2014**, *248*, 839–851.
7. Burke, A.F. Batteries and ultracapacitors for electric, hybrid, and fuel cell vehicles. *Proc. IEEE* **2007**, *95*, 806–820.
8. Bubna, P.; Advani, S.G.; Prasad, A.K. Integration of batteries with ultracapacitors for a fuel cell hybrid transit bus. *J. Power Sources* **2012**, *199*, 360–366.
9. Hu, X.; Johannesson, L.; Murgovski, N.; Egardt, B. Longevity-conscious dimensioning and power management of the hybrid energy storage system in a fuel cell hybrid electric bus. *Appl. Energy* **2015**, *137*, 913–924.
10. Odeim, F.; Roes, J.; Wülbeck, L.; Heinzel, A. Power management optimization of fuel cell/battery hybrid vehicles with experimental validation. *J. Power Sources* **2014**, *252*, 333–343.
11. Wang, X.; He, H.; Sun, F.; Sun, X.; Tang, H. Comparative study on different energy management strategies for plug-in hybrid electric vehicles. *Energies* **2013**, *6*, 5656–5675.
12. Han, J.; Charpentier, J.F.; Tang, T. An energy management system of a fuel cell/battery hybrid boat. *Energies* **2014**, *7*, 2799–2820.
13. Simmons, K.; Guezennec, Y.; Onori, S. Modeling and energy management control design for a fuel cell hybrid passenger bus. *J. Power Sources* **2014**, *246*, 736–746.
14. Maalej, K.; Kelouwani, S.; Agbossou, K.; Dubé, Y. Enhanced fuel cell hybrid electric vehicle power sharing method based on fuel cost and mass estimation. *J. Power Sources* **2014**, *248*, 668–678.
15. Andreasen, S.J.; Ashworth, L.; Sahlin, S.; Jensen, H.B.; Kær, S.K. Test of hybrid power system for electrical vehicles using a lithium-ion battery pack and a reformed methanol fuel cell range extender. *Int. J. Hydrog. Energy* **2014**, *39*, 1856–1863.
16. Ansarey, M.; Panahi, M.S.; Ziarati, H.; Mahjoob, M. Optimal energy management in a dual-storage fuel-cell hybrid vehicle using multi-dimensional dynamic programming. *J. Power Sources* **2014**, *250*, 359–371.
17. Thounthonga, P.; Raël, S.; Davat, B. Energy management of fuel cell/battery/supercapacitor hybrid power source for vehicle applications. *J. Power Sources* **2009**, *193*, 376–385.
18. Gao, D.; Jin, Z.; Lu, Q. Energy management strategy based on fuzzy logic for a fuel cell hybrid bus. *J. Power Sources* **2008**, *185*, 311–317.
19. Li, Q.; Chen, W.; Li, Y.; Liu, S.; Huang, J. Energy management strategy for fuel cell/battery/ultracapacitor hybrid vehicle based on fuzzy logic. *Int. J. Electr. Power Energy Syst.* **2012**, *43*, 514–525.
20. Paladini, V.; Donateo, T.; de Risi, A.; Laforgia, D. Super-capacitors fuel-cell hybrid electric vehicle optimization and control strategy development. *Energy Convers. Manag.* **2007**, *48*, 3001–3008.
21. Erdinc, O.; Vural, B.; Uzunoglu, M. A wavelet-fuzzy logic based energy management strategy for a fuel cell/battery/ultra-capacitor hybrid vehicular power system. *J. Power Sources* **2009**, *194*, 369–380.

22. Ayad, M.Y.; Becherif, M.; Henni, A. Vehicle hybridization with fuel cell, supercapacitors and batteries by sliding mode control. *Renew. Energy* **2011**, *36*, 2627–2634.
23. Amin; Bambang, R.T.; Rohman, A.S.; Dronkers, C.J.; Ortega, R.; Sasongko, A. Energy management of fuel cell/battery/supercapacitor hybrid power sources using Model Predictive Control. *IEEE Trans. Industr. Inform.* **2014**, *10*, 1192–2002.
24. Wipke, K.B.; Cuddy, M.R.; Burch, S.D. ADVISOR 2.1: A user-friendly advanced powertrain simulation using a combined backward/forward approach. *IEEE Trans. Veh. Technol.* **1999**, *48*, 1751–1761.
25. Guzzella, L.; Sciarretta, A. *Vehicle Propulsion Systems, Introduction to Modeling and Optimization*; Springer-Verlag: Berlin, Germany, 2005; pp. 13–17.
26. The Citaro FuelCELL Hybrid—Mercedes-Benz. Available online: http://www.mercedes-benz.de (accessed on 10 March 2015).
27. Emission Test Cycles: Manhattan Bus Cycle—DieselNet. Available online: http://www.dieselnet.com (accessed on 10 March 2015).
28. Gunther, S.; Ulbrich, S.; Hofmann, W. Driving cycle-based optimization of interior permanent magnet synchronous motor drives for electric vehicle application. In Proceedings of International Symposium on Power Electronics, Electrical Drives, Automation and Motion, Ischia, Italy, 18–20 June 2014; pp. 25–30.
29. Tazelaar, E.; Veenhuizen, B.; van den Bosch, P.; Grimminck, M. Analytical solution of the energy management for fuel cell hybrid propulsion systems. *IEEE Trans. Veh. Technol.* **2012**, *61*, 1986–1998.
30. Idaho National Engineering and Environmental Laboratory (INEEL). *FreedomCAR Battery Test Manual for Power-Assist Hybrid Electric Vehicles*; INEEL: Idaho Falls, ID, USA, 2003.
31. BMOD0500P016B02 Datasheet—Maxwell Technologies. Available online: http://www.maxwell.com (accessed on 10 March 2015).
32. Hegazy, O.; van Mierlo, J.; Lataire, P. Analysis, modeling, and implementation of a multidevice interleaved DC/DC converter for fuel cell hybrid electric vehicles. *IEEE Trans. Power Electron.* **2012**, *24*, 4445–4458.
33. Pukrushpan, J.T.; Stefanopoulou, A.G.; Peng, H. Modeling and control for PEM fuel cell stack system. In Proceedings of American Control Conference, Anchorage, AK, USA, 8–10 May 2002; pp. 3117–3122.
34. Boscaino, V.; Liga, R.; Miceli, R.; Cavallaro, C.; Raciti, A. Automotive brushless motor powered by fuel cell. In Proceedings of International Conference on Electrical Machines, Berlin, Germany, 2–5 September 2014; pp. 699–704.
35. Hu, X.; Li, S.; Peng, H. A comparative study of equivalent circuit models for Li-ion batteries. *J. Power Sources* **2012**, *198*, 359–367.
36. Devillers, N.; Jemei, S.; Péra, M.C.; Bienaimé, D.; Gustin, F. Review of characterization methods for supercapacitor modelling. *J. Power Sources* **2014**, *246*, 596–608.
37. Odeim, F.; Roes, J.; Heinzel, A. Power management optimization of a fuel cell/battery/supercapacitor hybrid system for transit bus applications. *IEEE Trans. Veh. Technol.* **2015**, under review.

38. Schiffer, J.; Bohlen, O.; de Doncker, R.W.; Sauer, D.U.; Young, A.K. Optimized energy management for fuelcell-supercap hybrid electric vehicles. In Proceedings of IEEE Vehicle Power and Propulsion Conference, Chicago, IL, USA, 7–9 September 2005; pp. 341–348.
39. Deb, K. *Multi-Objective Optimization Using Evolutionary Algorithms*; John Wiley & Sons Ltd.: Chichester, UK, 2001.
40. Gen, M.; Cheng, R. *Genetic Algorithms and Engineering Optimization*; John Wiley & Sons Ltd.: New York, NY, USA, 2000; pp. 97–115.
41. Fang, L.; Qin, S.; Xu, G.; Li, T.; Zhu, K. Simultaneous optimization for hybrid electric vehicle parameters based on multi-objective genetic algorithms. *Energies* **2011**, *4*, 532–544.
42. Global Optimization Toolbox, User's Guide—MathWorks. Available online: http://www.mathworks.com (accessed on 10 March 2015).
43. Marano, V.; Onori, S.; Guezennec, Y.; Rizzoni, G.; Madella, N. Lithium-ion batteries life estimation for plug-in hybrid electric vehicles. In Proceedings of IEEE Vehicle Power and Propulsion Conference, Dearborn, MI, USA, 7–10 September 2009; pp. 536–543.
44. Schmalstieg, J.; Käbitz, S.; Ecker, M.; Sauer, D.U. A holistic aging model for Li(NiMnCo)O_2 based 18650 lithium-ion batteries. *J. Power Sources* **2014**, *257*, 325–334.